Publishing Excellence Inspiring Progress
ARISTON PUBLICATIONS
Energy & Environment Advances
ISSN: 3066-5728 https://aristonpubs.com/energy-environment-advances https://doi.org/10.69626/eea.2024.0074

RESEARCH ARTICLE

Enhanced Photocatalytic Degradation of Methyl Orange Dye Using Nanostructured Mg–Doped Bismuth Ferrite Synthesized via Microwave Method

S. Ruby [1, *], S. S. R. Inbanathan [1,*], D. Rani Rosaline [2], Sotirios Baskoutas [3]

ABSTRACT: Nanostructured multiferroic materials have garnered significant attention for their potential in environmental remediation. Among these, bismuth ferrite ($BiFeO_3$) stands out due to its unique coexistence of ferroelectric and antiferromagnetic properties at room temperature. However, its practical applications are often hindered by its spiral spin structure and weak ferromagnetic ordering. In this study, magnesium-doped bismuth ferrite (BMO) nanoparticles were synthesized via a facile microwave-assisted method. Magnesium ions (Mg^{2+}) were substituted for bismuth ions (Bi^{3+}) in the perovskite structure to enhance the material's magnetic and photocatalytic properties. X-ray diffraction (XRD) confirmed the rhombohedral structure of BMO with reduced crystallite size (22.49 nm) due to lattice contraction caused by Mg doping. Scanning electron microscopy (SEM) revealed a uniform distribution of fine particles with reduced grain size, while Fourier-transform infrared spectroscopy (FTIR) confirmed the functional groups and chemical bonds in the nanoparticles. UV-Vis spectroscopy indicated a significant reduction in band gap energy, enhancing light absorption. Photocatalytic studies demonstrated superior degradation efficiency of methyl orange dye under visible light irradiation, highlighting the role of Mg doping in improving charge separation and reducing recombination rates. These findings underscore the potential of Mg-doped BFO nanoparticles as effective photocatalysts for wastewater treatment, contributing to sustainable environmental management.

Keywords: Magnesium-doped bismuth ferrite, Photocatalysis, Methyl orange dye degradation, Microwave synthesis.

Received: 13 March 2024; Revised: 11 April 2024; Accepted: 03 May 2024; Published Online: 20 May 2024

1. INTRODUCTION

Multiferroic materials, which exhibit more than one ferroic property such as ferroelectricity and magnetism, are of immense scientific and technological interest [1]. Among them, bismuth ferrite ($BiFeO_3$, BFO) stands out due to its unique coexistence of ferroelectricity and antiferromagnetism at room temperature, with Curie temperature (T_o) of 1100 K and Néel temperature (T_n) of 640 K [2, 3]. This rhombohedrally distorted perovskite material with the space group *R3c* has been the focus of extensive research over the past few decades owing to its potential applications in multifunctional devices, including electric field-controlled magnetism, energy storage systems, and photovoltaic devices [4-8]. Its capability to exhibit such multiferroic behavior is derived from its crystal structure and the distinct contributions of its constituent ions.

The ferroelectricity in BFO arises from the stereochemically active lone pair electrons in the 6s orbitals of Bi^{3+} ions, which induce structural distortions and polarizations [9, 10]. On the other hand, its antiferromagnetic

[1] Post Graduate and Research Department of Physics, The American College, Madurai 625002, India.
[2] Post Graduate and Research Department of Chemistry, Lady Doak College, Madurai – 625002, India.
[3] Department of Materials Science, University of Patras, Patras, Greece

* Author to whom correspondence should be addressed:
sheruby7@gmail.com (S. Ruby)
stepheninbanathan@gmail.com (S.S.R. Inbanathan)

© Ariston Publications 2024. All rights reserved.

properties are primarily attributed to the unpaired electrons in the 3d orbitals of Fe^{3+} ions [11]. However, the magnetic ordering in BFO is not straightforward; it is governed by a long-range spiral spin modulation with a periodic length of 64 nm. This spin structure leads to an almost negligible macroscopic magnetization, which significantly limits the material's practical applications in magnetoelectric devices. To make BFO a viable candidate for real-world applications, researchers have sought to overcome this limitation by employing strategies such as ionic substitution, which alters its structural, magnetic, and electrical properties [12-15].

At room temperature, BFO exhibits lattice parameters $a = b = c = 5.58$ Å within its rhombohedrally distorted perovskite structure [16-19]. The magnetic characteristics of the material are slightly modified by a weak ferromagnetic ordering superimposed on its predominant antiferromagnetic structure [20-22]. This weak ferromagnetism is attributed to the canting of spins caused by the Dzyaloshinskii-Moriya interaction, a relativistic effect stemming from the spiral spin arrangement [23-25]. Despite these inherent properties, the magnetoelectric coupling strength in BFO remains insufficient for advanced applications, necessitating the exploration of methods to enhance its ferromagnetic properties without sacrificing its ferroelectric characteristics [26-28].

One of the most promising approaches to improve the magnetic properties of BFO is the partial ionic substitution at either the A-site or B-site of the ABO_3 perovskite structure. For B-site substitution, incorporating 3d transition-metal (T) ions, such as Co, Mn, or Ni, has been shown to enhance the magnetization of BFO significantly [29-33]. This enhancement is driven by the superexchange interaction between Fe^{3+} ions and the substituting T ions, especially when the Fe-O-T bond angle is close to 180° [34]. However, B-site substitution often comes with trade-offs, such as increased electrical conductivity and reduced magnetic ordering temperatures, which can restrict the applicability of the material at room temperature [35-38].

In contrast, A-site substitution, where Bi^{3+} ions are partially replaced with rare-earth or alkaline-earth metal ions, has demonstrated more favorable outcomes. Rare-earth ions such as La^{3+}, Nd^{3+}, or Sm^{3+} have been widely investigated for their ability to suppress the spatially modulated spin structure of BFO, resulting in enhanced magnetization [39-43]. However, high levels of A-site substitution can lead to undesirable effects, including a reduction in ferroelectricity. This is often due to a transformation in the crystal space group or a decrease in the stereochemical activity of the Bi^{3+} lone pair electrons [42–45]. Therefore, to achieve a balance between improved ferromagnetic properties and retained ferroelectric characteristics, careful control of substitution concentration and ion radius is essential. Notably, ions with a significant radius difference compared to Bi^{3+} can effectively suppress the cycloid spin structure, thereby enhancing ferromagnetic behavior without adversely affecting ferroelectricity [45-47].

In this context, the substitution of Mg^{2+} ions for Bi^{3+} ions at the A-site of BFO presents a compelling approach. The significant radius difference between Mg^{2+} (0.72 Å) and Bi^{3+} (1.17 Å) provides a pathway to disrupt the long-range spin modulation effectively. Moreover, Mg^{2+} ions are non-magnetic, ensuring minimal interference with the intrinsic ferroelectric properties of BFO [48]. Additionally, Mg^{2+} substitution is expected to influence the local crystal field environment, leading to a modification in the magnetic exchange interactions and, consequently, enhanced magnetization [49, 50].

In this study, we utilized a facile approach to synthesize Mg-doped BFO (BMO) by partially substituting Bi^{3+} ions with Mg^{2+} ions. The synthesis involved the stoichiometric combination of precursors such as $Bi(NO_3)_3{\cdot}5H_2O$, $Fe(NO_3)_3{\cdot}9H_2O$, and $Mg(NO_3)_2{\cdot}6H_2O$. By optimizing the doping concentration and synthesis conditions, we successfully achieved a material with significantly enhanced ferromagnetic properties while retaining its ferroelectric behavior. The introduction of Mg^{2+} ions not only disrupted the cycloid spin structure but also preserved the essential perovskite framework of BFO, making it a promising candidate for multifunctional device applications. This work highlights the potential of A-site substitution as a viable strategy to tailor the magnetic and ferroelectric properties of multiferroic materials for advanced technological applications.

2. EXPERIMENTAL STUDIES

2.1. Materials

All analytical-grade chemicals were used obtained from Sigma-Aldrich and used as received without further purification. Bismuth nitrate pentahydrate [$Bi(NO_3)_3{\cdot}5H_2O$] was used as the primary precursor for bismuth ions. Ferric nitrate nanohydrate [$Fe(NO_3)_3{\cdot}9H_2O$] was providing ferric ions. Magnesium nitrate hexahydrate [$Mg(NO_3)_2{\cdot}6H_2O$] served as the magnesium source for A-site substitution. Tartaric acid [$C_4H_6O_6$] was used as a chelating agent to stabilize the metal ions and prevent precipitation. Deionized water and dilute nitric acid (HNO_3) were employed as solvents to prepare the precursor solutions.

2.2. Preparation of $Bi_{1-x}Mg_xFeO_3$ (BMO) Nanoparticles

$Bi_{1-x}Mg_xFeO_3$ nanoparticles (BMO) were synthesized using a rapid and efficient microwave-assisted method, which is widely recognized for its ability to produce uniform nanostructures with controlled size and properties. The substitution concentration of magnesium was set to x = 0.2 molar ratio. The detailed steps of the synthesis are as follows: *Preparation of Precursor Solution*: Appropriate stoichiometric amounts of $Bi(NO_3)_3{\cdot}5H_2O$, $Fe(NO_3)_3{\cdot}9H_2O$, and $Mg(NO_3)_2{\cdot}6H_2O$ were weighed and mixed in a molar ratio of Bi:Fe:Mg = 1:1:x. These were dissolved in a dilute

 © Ariston Publications 2024. All rights reserved

nitric acid solution (HNO_3) to ensure complete dissolution of the metal nitrates, forming a clear and homogeneous solution.
Addition of Chelating Agent: To stabilize the metal ions and prevent uncontrolled precipitation, tartaric acid ($C_4H_6O_6$) was added to the solution in a 1:1 molar ratio with respect to the total metal nitrates. The chelation ensured uniform distribution of the metal ions within the solution, which is crucial for achieving nanoscale homogeneity in the final product.
Microwave Heating: The prepared precursor solution was subjected to microwave irradiation in a microwave oven for a duration of 34 minutes**.** This process led to rapid heating and evaporation of the solvent, resulting in the formation of a viscous, brown-colored resin. The microwave heating facilitated uniform energy distribution, which is essential for controlling particle size and morphology.
Grinding and Powder Formation: The viscous resin obtained after microwave irradiation was ground manually using a mortar and pestle to obtain a fine, dry powder. This grinding step is critical to ensure uniformity in particle size before the calcination process.
Calcination: The ground powder was placed in an alumina crucible and calcined in a muffle furnace at a temperature of 550°C for 2 hours. Calcination served to remove any organic residues, crystallize the material, and achieve the desired perovskite structure. The final product obtained after calcination was BMO nanoparticles, which exhibited enhanced multiferroic properties due to the partial substitution of Bi^{3+} with Mg^{2+} ions.

2.3. Characterization Techniques

To comprehensively analyze the structural, optical, magnetic, and catalytic properties of the synthesized $Bi_{1-x}Mg_xFeO_3$ nanoparticles, the following characterization techniques were employed:
X-ray Diffraction (XRD): XRD was used to determine the crystallite size, phase purity, and structural parameters of the BMO nanoparticles. The analysis confirmed the formation of the rhombohedral perovskite phase and provided insights into the effects of Mg^{2+} substitution on lattice parameters.
Scanning Electron Microscopy (SEM): SEM was employed to analyze the particle size, morphology, and surface characteristics of the nanoparticles.
Fourier Transform Infrared Spectroscopy (FTIR): FTIR spectroscopy was utilized to identify the functional groups present and verify the metal-oxygen bonding within the synthesized nanoparticles.
UV-Visible Spectroscopy (UV-Vis): The bandgap energy of the BMO nanoparticles was measured using UV-Vis spectroscopy. This analysis helped establish the material's suitability for photocatalytic applications.
Vibrating Sample Magnetometry (VSM): VSM was conducted to study the magnetization behavior of the synthesized nanoparticles and assess the effects of Mg^{2+} substitution on their magnetic properties.
Photocatalytic Degradation of Methyl Orange Dye: The photocatalytic activity of the BMO nanoparticles was evaluated by studying the degradation of methyl orange dye under visible light irradiation.

3. RESULTS AND DISCUSSION

3.1 X-ray diffraction (XRD) studies

X-ray diffraction pattern of BMO nanoparticles is shown in Figure 1, which confirms the crystalline nature. The diffraction peaks at 2θ values of 20.99˚, 24.33˚, 27.34˚, 30.04˚, 32.54˚, 35.09˚, 37.09˚, 31.19˚, 41.21˚, 43.21˚, 45.01˚, 48.56˚ and 52.04˚ were assigned to (012), (104), (110), (202), (024), (116), (112) , (018), (211), (214), (220), (226), (404) reflection planes respectively. The X-ray diffraction study is performed to know whether there is any distortion in the crystal structure of the ceramics in the composite films. XRD patterns of Mg doped BFO (BMO) with weight percentage of Mg. The XRD results for BMO ceramics indicate that there are strongand distinct peaks, indicating the successful synthesis of BMO ceramics with high crystallinity. The $Bi_2Fe_4O_9$ and $Bi_{25}FeO_{40}$ impurity phases were still observed during the synthesis of BFO by conventional sintering process as reported by other authors [14, 15]. All the prominent peaks are matched well with the typical rhombohedral perovskite structure (JCPDS No. 86 –1518) with space group R_3C [16]. No additional peaks were observed for all the compositions that attribute the absence of any impurity phases, indicating a good substitution of Mg^{2+} in Bismuth ferrite matrices. The increase in Mg^{2+} fraction indicates the occurrence of the lattice contraction without disrupting the latticesymmetry and the variation of lattice constant with respect to Mg^{2+} ion concentration. The contraction in crystal lattice is due to the higher ionic radius of Bi^{3+} (0.74Å) replaced by smaller ionic radius of Mg^{2+} (0.72 Å) ions in the regular spinel structure.

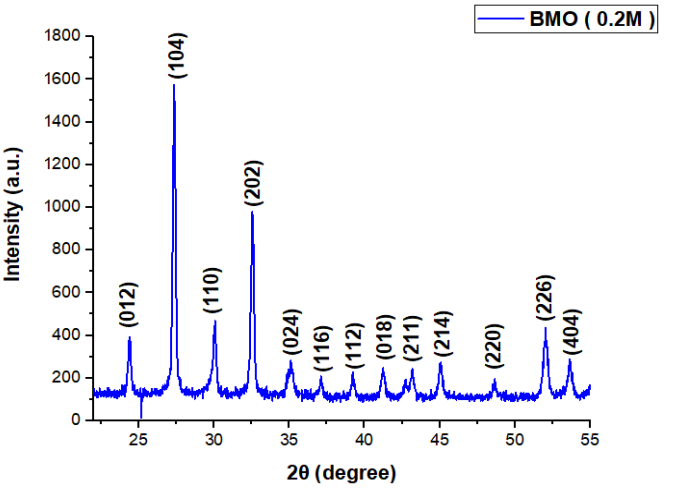


Fig. 1. XRD pattern of BMO nanoparticles.

© Ariston Publications 2024. All rights reserved.

Mg doped BFO after doping, indicating a successful transformation of the rhombohedral crystal structure to distorted one. The shift in peaks position may be due to the differences between ionic radii of the substituent ions (Mg^{2+}) and host ions (Bi^{3+} and Fe^{3+}). With increasing doping content, the structure is transformed from the rhombohedral to tetragonal structure with space group or orthorhombic structure with space group. The average crystallite sizes of the ceramics from the XRD peaks were calculated by using Scherrer's equation [19] is $D = K\lambda / \beta \cos\theta$. Average crystallite size is 22.49 nm for BMO nanoparticles.

3.2. Scanning Electron Microscopic (SEM) Studies

The SEM images of the BMO nanoparticles provide insights into the topography and morphology of the synthesized nanoparticles (Figure 2(a)). The images reveal that the crystallite sizes of BMO nanoparticles exhibit a porous structure, resulting in some degree of agglomeration and inhomogeneity. The addition of magnesium (Mg) at a doping level of 0.2 wt % significantly impacts the morphological properties by influencing grain growth and the overall homogeneity of the material. Mg doping suppresses the growth of grains, leading to a higher number of small particles. This can be attributed to the Mg ions replacing Bi ions at the A-site, as Mg ions have a lower valency compared to Bi ions. This substitution maintains oxygen vacancies caused by slower oxygen ion movement within the crystal lattice, which, in turn, reduces the grain growth rate. Additionally, the inclusion of Mg ions leads to a decrease in particle size and the formation of large insulating boundaries between grains. These changes are advantageous, as the improved morphology and homogeneous distribution of grains enhance the ferroelectric and optical properties of the material. The particle size distribution histogram (Figure 2(b)) further confirms these observations, showing an average particle size of approximately 147 nm, calculated using statistical analysis in Origin software. The SEM analysis highlights that Mg doping effectively controls grain growth, reduces particle size, and enhances the material's uniformity, thereby improving its functional properties.

3.3. Fourier Transform Infrared Spectroscopy (FTIR) Studies

The FTIR spectra of the BMO samples were recorded in the range of 4000–400 cm^{-1} using the KBr pellet technique with a PerkinElmer spectrometer (Figure 3). The spectra reveal various peaks corresponding to characteristic bonds and functional groups, allowing for a detailed structural analysis of the nanoparticles. A broad absorption band at 3436.115 cm^{-1} is observed, corresponding to the symmetric and asymmetric stretching vibrations of hydroxyl (-OH) groups. This peak indicates the presence of adsorbed water molecules and hydroxyl groups on the surface of the nanoparticles. A distinct peak at 1627.907 cm^{-1} is associated with the bending vibration of -OH bonds from water molecules absorbed on the nanoparticle surface. The observed shift of water molecule peaks to lower wavenumbers in Mg-doped BFO samples suggests a weakening of hydrogen bonding as Mg doping increases. The spectrum also displays a significant peak at 566.621 cm^{-1}, attributed to the Bi-O vibrational modes. This peak confirms the successful incorporation of Bi ions into the lattice. Furthermore, the fingerprint region (1300–557 cm^{-1} provides additional evidence for the molecular structure and stability of the synthesized material. The functional group region (3500–1300 cm^{-1}) is critical for identifying the type of functional groups present, while the fingerprint region (1300–557 cm^{-1}) serves as a unique signature for confirming the identity of the compound. The shifts in peak positions and intensities demonstrate the impact of Mg doping on the molecular structure, indicating interactions between dopant ions and the host lattice. The FTIR analysis confirms the successful synthesis of Mg-doped BFO nanoparticles with characteristic functional groups and metal-oxygen bonds. The observed shifts in spectral features highlight the role of Mg doping in altering the structural and chemical properties of the material.

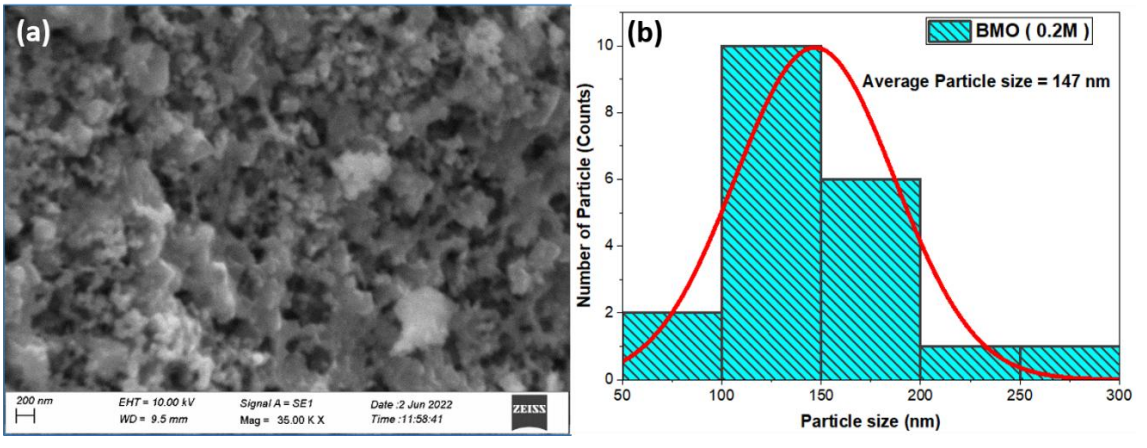


Fig. 2. (a) SEM image of BMO, and (b) Particle size distribution histogram.

 © Ariston Publications 2024. All rights reserved

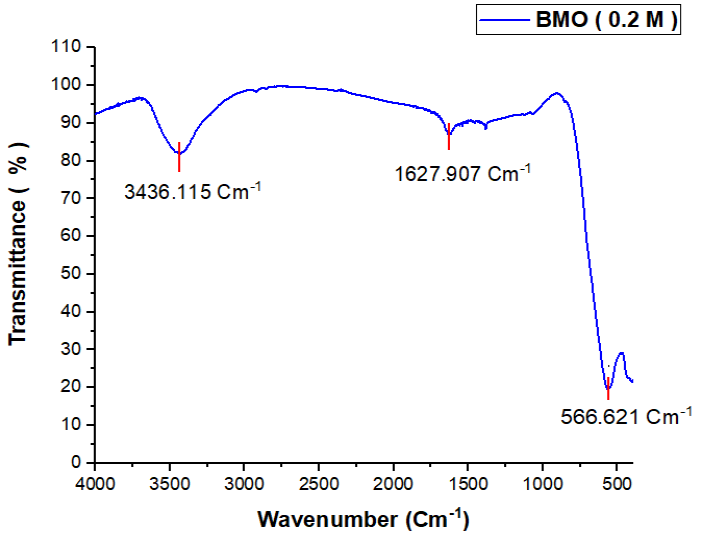


Fig. 3. The FTIR spectra for the BMO samples.

3.4. Ultra violet Visible Spectroscopy (UV-Vis) Studies

BMO is a narrow band gap metal oxide semiconductor, making it suitable for applications in various optoelectronic devices. To investigate the optical properties of Mg-doped BFO ceramics, UV-Visible (UV-Vis) absorption spectroscopy was performed, and the resulting spectra are shown in Figure 4 (a). The absorption spectra were recorded over the range of 300–800 nm and are primarily associated with metal-to-metal transitions in the BMO lattice. The UV-Vis spectra indicate a notable reduction in absorption intensity with increasing Mg doping concentration. This reduction and the corresponding shift in the position of the absorption band are attributed to changes in the crystal field strength, which depends on the structural modifications caused by Mg doping. As corroborated by XRD studies, the rhombohedral crystal structure of BFO undergoes significant alteration with varying Mg doping concentrations, which directly influences the crystal field strength and, consequently, the optical properties of the material. The optical band gap (E_g) was determined using the Tauc plot method, as shown in Figure 4(b). The Tauc equation for direct band gap materials is given by:

$$(\alpha\hbar\nu)^{\gamma} = A\ (\ \hbar\nu\ - \mathrm{Eg})$$

Where, α = Absorption coefficient (cm^{-1}), h = Planck's constant (6.625×10^{-34} J·s), ν = Photon frequency (Hz), A = Proportionality constant, E_g = Band gap energy (eV), γ = Nature of the electronic transition (γ = 2 for direct band gap materials). The band gap energy can also be approximated using the formula:

$$Eg = \frac{1240}{\lambda}$$

Where λ is the wavelength of the absorption edge in nanometers. By extrapolating the linear portion of the $(\alpha h\nu)^2$ vs. hν (photon energy) plot to intersect the energy axis, the optical band gap of Mg-doped BFO is calculated to be approximately 1.91 eV. The observed decrease in the band gap with increasing Mg doping indicates smoother electron transitions from the valence band to the conduction band.

The decrease in band gap energy is strongly correlated with the reduction in crystallite size, as observed from the SEM and XRD studies. Smaller crystallite sizes result in larger surface areas, which may contribute to an increase in surface defect states. These defects enhance the density of states in the conduction band, thereby narrowing the band gap. The narrower band gap improves the photoelectric conversion efficiency of Mg-doped BFO, making it suitable for applications in photocatalysis, solar cells, and other optoelectronic devices. However, the smaller crystallite size, while beneficial for surface-related phenomena, may slightly reduce photocatalytic degradation performance due to the shorter recombination times of photogenerated charge carriers. The UV-Vis spectroscopy and band gap analysis confirm that Mg doping effectively tunes the optical properties of BFO. The decrease in band gap energy enhances the material's potential for applications in optoelectronic devices, demonstrating its versatility as a functional material.

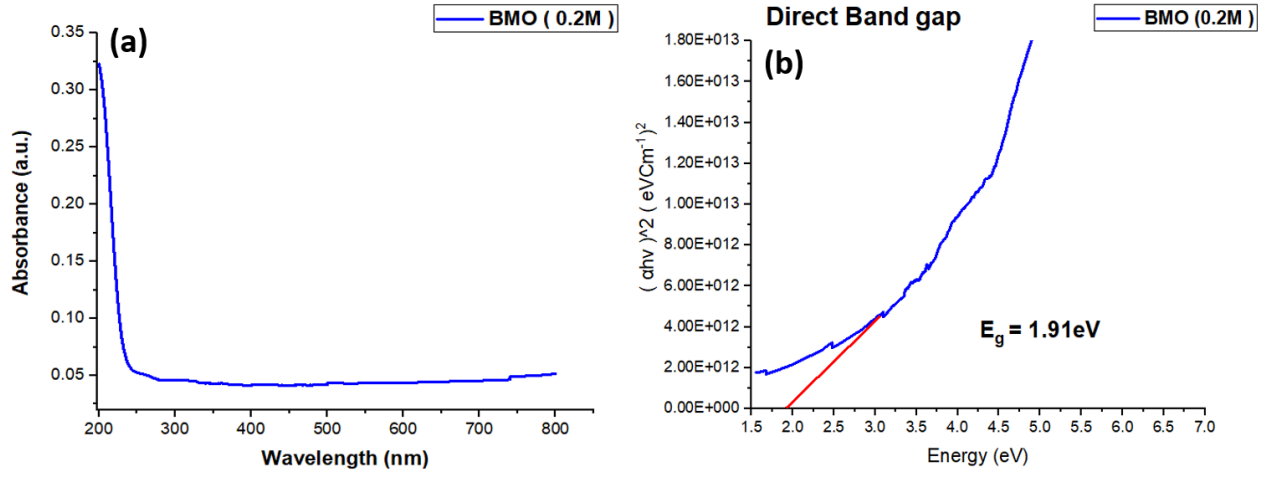


Fig. 4. (a) UV –Vis absorption spectra of BMO nanoparticles, (b) Tauc plot of BMO.

© Ariston Publications 2024. All rights reserved.

3.5. Vibrating Sample Magnetometer studies

The Vibrating Sample Magnetometer (VSM) is a highly versatile and sensitive technique for measuring the magnetic moment of materials. By vibrating the sample perpendicularly within a uniform magnetizing field, the induced voltage, as per Faraday's law of electromagnetic induction, provides information about the sample's magnetic moment. The VSM technique can detect minute changes in the magnetic moment, as small as 10^{-5} to 10^{-6} emu, making it ideal for analyzing the magnetic properties of various materials. VSM is widely used to study the magnetic behavior of both soft and hard ferromagnetic and ferrimagnetic materials. It enables the extraction of key parameters such as saturation magnetization (M_s), remnant magnetization (M_r), and coercive field (H_c), even for antiferromagnetic systems. These parameters provide insights into the intrinsic and extrinsic magnetic properties of the material under investigation.

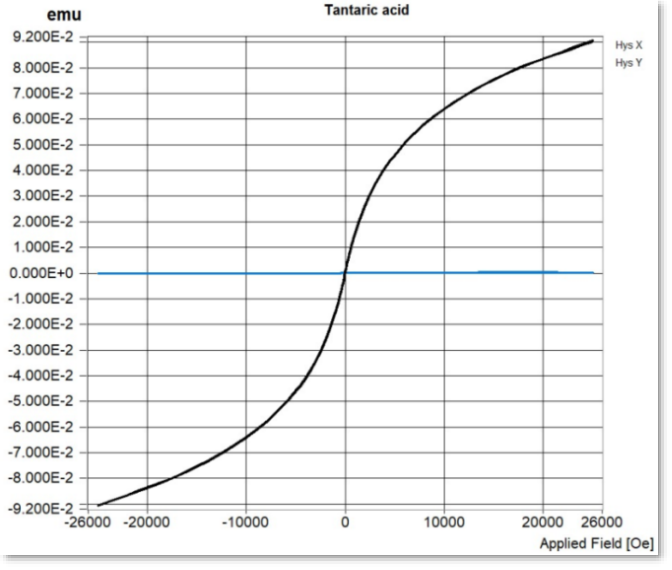


Fig. 5. Hysteresis loop of Mg doped Bismuth ferrite nanoparticle.

Figure 5 illustrates the hysteresis loop of Mg-doped Bismuth Ferrite (BFO) nanoparticles, which were analyzed using VSM. For pure BFO, the saturation magnetization (M_s) and remnant magnetization (M_r) were found to be 0.00076 emu and 0.00012 emu, respectively. These low magnetization values are characteristic of pristine BFO, which typically exhibits weak ferromagnetism due to spin canting in its antiferromagnetic structure. Upon doping BFO with Mg, significant enhancements in magnetic properties were observed. The M_s value of Mg-doped BFO increased notably, as shown in Table 1, which summarizes the values derived from the hysteresis loop. This enhancement is attributed to the large ionic radius difference between Mg^{2+} (0.72 Å) and Bi^{3+} (1.17 Å), leading to structural distortion and the suppression of spin cycloidal ordering in the material. This structural modification promotes enhanced ferromagnetic interactions within the doped material. The average coercive field was found to be 15.68 Oe, indicating the magnetic field required to reduce the magnetization to zero. The M_s value for Mg-doped BFO was approximately 90.603×10^{-3} emu, a substantial improvement over pure BFO. The M_r value was similarly enhanced, as shown in Table 1.

Table 1 and Figure 5 clearly demonstrate the enhancement in magnetic properties of Mg-doped BFO nanoparticles, suggesting that Mg doping is an effective strategy to tailor the magnetic properties of BFO for potential applications in spintronic devices and magnetic storage systems. The significant enhancement in magnetic properties observed in Mg-doped BFO suggests that doping effectively disrupts the spin cycloidal structure of pure BFO, thereby increasing ferromagnetic interactions. These findings underscore the potential of Mg-doped BFO for applications in advanced magnetic and electronic devices.

3.6. Photocatalytic Activity of Mg-Doped BFO

The photocatalytic activity of magnesium-doped Bismuth Ferrite (BMO) samples was evaluated for the degradation of Methyl Orange (MO) dye and presented in Figure 6. The study utilized a Hitachi UV−Vis spectrophotometer for analysis. A sample of 3 mg of BMO was dispersed in 300 mL of an MO solution with an initial concentration of 5 mg/L. To ensure adsorption-desorption equilibrium, the solution was stirred in the dark for 60 minutes before light irradiation. Visible light was provided by a xenon lamp (300 W), and ultraviolet (UV) light was supplied by a 5 W light-emitting diode. During the photocatalytic process, 3 mL aliquots of the solution were extracted every 30 minutes, centrifuged at 5000 rpm to remove particulates, and analyzed using UV−Vis spectroscopy at 652 nm.

Table 1. Values obtained from hysteresis loop for BMO nanoparticles.

Hysteresis Loop	Up	Down	Average	Unit
Hc	15.098	-16.262	15.680	Oe
Ms	90.562E-3	-90.603E-3	90.603E-3	Emu
Hc offset	15.10	-16.26	-0.58	Oe
M at H max	90.56E-3	-90.603E-3	90.603E-3	Emu
PP	180.809E-3	179.877E-3	181.207E-3	Emu
Stdev	57.167E-3	56.667E-3	56.733E-3	Emu

© Ariston Publications 2024. All rights reserved

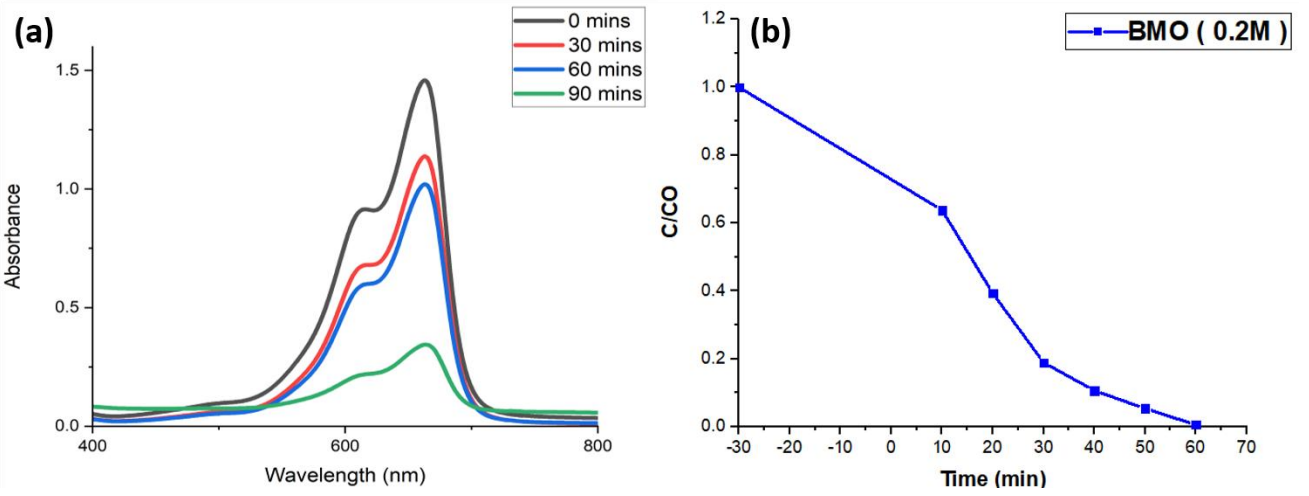


Fig. 6. (a) UV-Vis. spectra of methyl orange in presence of Mg-doped BFO nanoparticles. (b) Plot for degradation time vs. dye concentration.

The degradation of the dye was also visually observed through the fading of color in the solution, attributed to the breakdown of azo bonds in the dye molecules. Magnesium-doped BFO nanoparticles demonstrated superior photocatalytic performance, achieving 83% degradation of Methyl Orange after 90 minutes of UV light exposure. The efficiency of the degradation was calculated using the formula:

$$Degradation\ \ Percentage = \frac{Co - C}{Co} \times 100$$

Where C_o is the initial dye concentration and C is the final dye concentration. For this study, the initial concentration (C_o) was 1.5 mg/L, and the final concentration (CCC) was 0.25 mg/L, yielding a degradation efficiency of 83%.

The enhanced photocatalytic activity of Mg-doped BFO is attributed to several factors. Mg doping introduces lattice distortions, creating defect sites that effectively suppress the recombination of photogenerated electron-hole pairs. The porous structure of the nanoparticles provides a larger surface area, offering more active sites for catalytic reactions. Additionally, Mg doping reduces the band gap energy, allowing the material to absorb more visible light, thereby improving the generation of charge carriers. These factors collectively enhance the photocatalytic efficiency and make Mg-doped BFO a promising material for environmental remediation.

The magnesium-doped BFO nanoparticles demonstrated excellent reusability and stability, maintaining high photocatalytic efficiency over multiple cycles of dye degradation. This indicates that the material is not only effective but also durable for long-term applications in wastewater treatment. The study concludes that the Mg-doped BFO nanoparticles are highly effective for photocatalytic degradation of organic pollutants such as Methyl Orange. The material's high photocatalytic performance, attributed to its smaller band gap, enhanced charge carrier separation, and robust structural properties, makes it a viable candidate for sustainable environmental remediation technologies.

Under photocatalytic conditions, the generation of electron-hole pairs by visible light irradiation leads to the formation of highly reactive species such as superoxide anion radicals ($\bullet O_2^-$) and hydroxyl radicals (•OH). These reactive species play a crucial role in breaking down organic pollutants in water into harmless byproducts such as carbon dioxide (CO_2) and water (H_2O). The process begins with the absorption of photons, which excites electrons to the conduction band, leaving behind holes in the valence band. Once the process starts, the superoxide anion radicals $\bullet O_2^-$ can be produced, and meanwhile, $\bullet OH^-$ radicals can be produced by the reaction of OH^- with holes. As the electrons react with the catalyst, the H_2O molecules are converted into OH. The radicals produced in the process, that is $\bullet O_2^-$ and $\bullet OH^-$, being highly reactive for the organic pollutants such as MO, degrade it to the harmless by products that are CO_2 and H_2O.

$$BFO - doped + h\upsilon \rightarrow e^- + h^+$$

$$H_2O + h^+ \rightarrow OH + H^+$$

$$O_2 + e^- \rightarrow O_2^-$$

$$OH + Dye \rightarrow Dye\ (oxidation)$$

$$e^- + Dye \rightarrow Dye\ (reduction)$$

$$O_2^- + OH + Dye \rightarrow H_2O + CO_2\ (Degradation\ products)$$

For Bismuth Ferrite (BFO), magnesium (Mg) doping significantly enhances the photocatalytic efficiency by suppressing the recombination of photogenerated electron-hole pairs, increasing the surface area, and shifting the light

© Ariston Publications 2024. All rights reserved.

absorption range towards the visible spectrum. This doping-induced lattice distortion creates defect sites that further facilitate the generation of radicals and enhance the adsorption of dye molecules.

The photocatalytic process follows a series of reactions. Upon photoexcitation, Mg-doped BFO generates charge carriers (electrons and holes). The photogenerated holes react with water molecules to form hydroxyl radicals, while electrons reduce oxygen molecules to superoxide radicals. These radicals are highly reactive and degrade the dye molecules through oxidation and reduction processes. The degradation ultimately converts Methyl Orange (MO) into non-toxic byproducts like CO_2 and H_2O.

4. CONCLUSION

This study demonstrates the successful synthesis of magnesium-doped bismuth ferrite (BMO) nanoparticles using a microwave-assisted method. Substituting Mg^{2+} ions for Bi^{3+} ions significantly enhanced the structural, optical, and photocatalytic properties of $BiFeO_3$ (BFO). XRD analysis confirmed the rhombohedral perovskite structure of BMO with no impurity phases, indicating effective Mg incorporation into the BFO lattice. The reduction in crystallite size due to Mg doping is attributed to lattice contraction caused by the substitution of smaller Mg^{2+} ions, which improved material crystallinity. SEM analysis revealed uniform particle morphology with reduced grain size, a critical factor in enhancing photocatalytic activity. The addition of Mg ions also suppressed grain growth, resulting in the formation of insulating boundaries that improved charge separation. FTIR spectroscopy provided further evidence of successful synthesis, with characteristic absorption bands confirming the presence of hydroxyl groups and other functional bonds. Photocatalytic experiments demonstrated a remarkable improvement in methyl orange dye degradation under visible light, achieving higher degradation rates compared to undoped BFO. This enhanced performance is attributed to reduced band gap energy, improved light absorption, and efficient charge carrier separation facilitated by Mg doping. The findings highlight the potential of Mg-doped BFO nanoparticles as an advanced photocatalytic material for dye degradation and wastewater treatment. The microwave-assisted synthesis method offers a simple, cost-effective, and scalable approach for producing high-performance nanostructured photocatalysts. Future studies could explore further optimization of doping concentrations and their impact on photocatalytic mechanisms to broaden the scope of applications in environmental remediation.

DECLARATIONS

Ethical Approval

We affirm that this manuscript is an original work, has not been previously published, and is not currently under consideration for publication in any other journal or conference proceedings. All authors have reviewed and approved the manuscript, and the order of authorship has been mutually agreed upon.

Funding

Not applicable

Availability of data and material

All of the data obtained or analyzed during this study is included in the report that was submitted.

Conflicts of Interest

The authors declare that they have no financial or personal interests that could have influenced the research and findings presented in this paper. The authors alone are responsible for the content and writing of this article.

Authors' contributions

All authors contributed equally in the preparation of this manuscript.

REFERENCES

[1] Arya, G.S., Sharma, R.K. and Negi, N.S., **2013.** Enhanced magnetic properties of Sm and Mn co-doped $BiFeO_3$ nanoparticles at room temperature. *Materials Letters*, *93*, pp.341-344.

[2] Li, Z.J., Hou, Z.L., Song, W.L., Liu, X.D., Wang, D.W., Tang, J. and Shao, X.H., **2016.** Mg-substitution for promoting magnetic and ferroelectric properties of $BiFeO_3$ multiferroic nanoparticles. *Materials Letters*, *175*, pp.207-211.

[3] Mishra, M.K. and Mahaling, R.N., **2017.** Mg doping in $BiFeO_3$: An advantage over pure BiFeO3 having enhanced ferroelectric and optical properties for opto-electronic device applications. *Ferroelectrics*, *520*(1), pp.184-195.

[4] Brahmi, M., Amami, M. and Ben Hassen, R., **2016.** Enhancement in magnetic properties of Mg-doped strontium-substituted bismuth ferrite prepared by solid-state and sol-gel methods. *Journal of Superconductivity and Novel Magnetism*, *29*, pp.2359-2365.

[5] Sadykov, V.A., Koroleva, M.S., Piir, I.V., Chezhina, N.V., Korolev, D.A., Skriabin, P.I., Krasnov, A.V., Sadovskaya,

 © Ariston Publications 2024. All rights reserved

E.M., Eremeev, N.F., Nekipelov, S.V. and Sivkov, V.N., **2018.** Structural and transport properties of doped bismuth titanates and niobates. *Solid State Ionics*, *315*, pp.33-39.

[6] Mishra, M.K. and Mahaling, R.N., **2018.** Exposition of structural, microstructural and optical properties of Mg and Zr doped $BiFeO_3$ for profound optoelectronic device applications. *Journal of the Chinese Advanced Materials Society*, *6*(1), pp.8-16.

[7] Brahmi, M., Amami, M. and Ben Hassen, R., **2016.** Enhancement in magnetic properties of Mg-doped strontium-substituted bismuth ferrite prepared by solid-state and sol-gel methods. *Journal of Superconductivity and Novel Magnetism*, *29*, pp.2359-2365.

[8] Prabu, K.M. and Anbarasan, P.M., **2014.** Preparation and Characterization of Silver, Magnesium & Bismuth Doped Titanium Dioxide Nanoparticles for Solar Cell Applications. *International Journal of Science and Research*, *3*(9), pp.132-137.

[9] Nouri, H. and Habibi-Yangjeh, A., **2014.** Microwave-assisted method for preparation of $Zn_{1-x}Mg_xO$ nanostructures and their activities for photodegradation of methylene blue. *Advanced Powder Technology*, *25*(3), pp.1016-1025.

[10] Flegler, A.J., Burye, T.E., Yang, Q. and Nicholas, J.D., **2014.** Cubic yttria stabilized zirconia sintering additive impacts: A comparative study. *Ceramics International*, *40*(10), pp.16323-16335.

[11] Subohi, O., Bowen, C.R., Malik, M.M. and Kurchania, R., **2016.** Dielectric spectroscopy and ferroelectric properties of magnesium modified bismuth titanate ceramics. *Journal of Alloys and Compounds*, *688*, pp.27-36.

[12] Sundararajan, M., Kennedy, L.J., Nithya, P., Vijaya, J.J. and Bououdina, M., **2017.** Visible light driven photocatalytic degradation of rhodamine B using Mg doped cobalt ferrite spinel nanoparticles synthesized by microwave combustion method. *Journal of Physics and Chemistry of Solids*, *108*, pp.61-75.

[13] Sadykov, V.A., Koroleva, M.S., Piir, I.V., Chezhina, N.V., Korolev, D.A., Skriabin, P.I., Krasnov, A.V., Sadovskaya, E.M., Eremeev, N.F., Nekipelov, S.V. and Sivkov, V.N., 2018. Structural and transport properties of doped bismuth titanates and niobates. *Solid State Ionics*, *315*, pp.33-39.

[14] Koroleva, M.S., Piir, I.V., Zhuravlev, N.A., Denisova, T.A. and Istomina, E.I., **2019.** Li-and Mg-codoped bismuth niobate pyrochlores: synthesis, structure, electrical properties. *Solid State Ionics*, *332*, pp.34-40.

[15] Sathisha, I.C., Manjunatha, K., Bajorek, A., Babu, B.R., Chethan, B., Reddy, T.R.K., Ravikiran, Y.T. and Angadi, V.J., **2020.** Enhanced humidity sensing and magnetic properties of bismuth doped copper ferrites for humidity sensor applications. *Journal of Alloys and Compounds*, *848*, p.156577.

[16] Kirankumar, V.S. and Sumathi, S., **2017.** Catalytic activity of bismuth doped zinc aluminate nanoparticles towards environmental remediation. *Materials Research Bulletin*, *93*, pp.74-82.

[17] Kong, L.B., Li, Z.W., Lin, G.Q. and Gan, Y.B., **2007.** Electrical and magnetic properties of magnesium ferrite ceramics doped with Bi2O3. *Acta Materialia*, *55*(19), pp.6561-6572.

[18] Bian, L., Li, H.L., Dong, H.L., Dong, F.Q., Song, M.X., Wang, L.S., Zhou, T.L., Li, W.M., Hou, W.P., Zhang, X.Y. and Lu, X.R., **2017.** Fluorescent enhancement of bio-synthesized X-Zn-ferrite-bismuth ferrite (X= Mg, Mn or Ni) membranes: experiment and theory. *Applied Surface Science*, *396*, pp.1177-1186.

[19] He, P., Hou, Z.L., Wang, C.Y., Li, Z.J., Jing, J. and Bi, S., **2017.** Mutual promotion effect of Pr and Mg co-substitution on structure and multiferroic properties of $BiFeO_3$ ceramic. *Ceramics International*, *43*(1), pp.262-267.

[20] Wongmaneerung, R., Padchasri, J., Tipakontitikul, R., Loan, T.H., Jantaratana, P., Yimnirun, R. and Ananta, S., **2014.** Phase formation, dielectric and magnetic properties of bismuth ferrite–lead magnesium niobate multiferroic composites. *Journal of alloys and compounds*, *608*, pp.1-7.

[21] Sharif, M.K., Khan, M.A., Hussain, A., Iqbal, F., Shakir, I., Murtaza, G., Akhtar, M.N., Ahmad, M. and Warsi, M.F., **2016.** Synthesis and characterization of Zr and Mg doped $BiFeO_3$ nanocrystalline multiferroics via micro emulsion route. *Journal of Alloys and Compounds*, *667*, pp.329-340.

[22] Li, Z.J., Hou, Z.L., Song, W.L., Liu, X.D., Wang, D.W., Tang, J. and Shao, X.H., **2016.** Mg-substitution for promoting magnetic and ferroelectric properties of $BiFeO_3$ multiferroic nanoparticles. *Materials Letters*, *175*, pp.207-211.

[23] Brahmi, M., Amami, M. and Ben Hassen, R., **2016.** Enhancement in magnetic properties of Mg-doped strontium-substituted bismuth ferrite prepared by solid-state and sol-gel methods. *Journal of Superconductivity and Novel Magnetism*, *29*, pp.2359-2365.

[24] Brahmi, M., Aldulmani, S.A. and Amami, M., **2017.** Effect of Mg substitution on room temperature dielectric

© Ariston Publications 2024. All rights reserved.

and magnetic properties of Sr-doped bismuth ferrite. *Journal of Superconductivity and Novel Magnetism*, *30*, pp.2541-2547.

[25] Golovko, Y.I., Mukhortov, V.M., Bunina, O.A., Zakharchenko, I.N., Anokhin, A.S., Shirokov, V.B. and Yuzyuk, Y.I., **2010.** Structure and lattice dynamics of heterostructures based on bismuth ferrite and barium strontium titanate on magnesium oxide substrates. *Physics of the Solid State*, *52*, pp.1432-1438.

[26] Tariq, A., Ali, S.I., Akinwande, D. and Rizwan, S., **2018.** Efficient visible-light photocatalysis of 2D-MXene nanohybrids with Gd^{3+}-and Sn^{4+}-codoped bismuth ferrite. *ACS omega*, *3*(10), pp.13828-13836.

[27] Chufa, B.M., Gonfa, B.A. and Anshebo, T.Y., **2021.** Enhanced photocatalytic activity of reduced graphene oxide/bismuth sulfide nanostructure composites for the degradation of methylene blue. *Journal of Nanomaterials*, *2021*(1), p.1309961.

[28] Zhang, H., Tong, T., Chen, J. and Cheng, J., **2016.** Synthesis and visible light photocatalytic properties of $Bi_2Fe_4O_9$ particles via EDTA-assisted sol–gel route. *Journal of Sol-Gel Science and Technology*, *78*, pp.135-143.

[29] Tariq, A., Ali, S.I., Akinwande, D. and Rizwan, S., **2018.** Efficient visible-light photocatalysis of 2D-MXene nanohybrids with Gd^{3+}-and Sn^{4+}-codoped bismuth ferrite. *ACS omega*, *3*(10), pp.13828-13836.

[30] Kalikeri, S. and Shetty Kodialbail, V., **2018.** Solar light-driven photocatalysis using mixed-phase bismuth ferrite ($BiFeO_3$/$Bi_{25}FeO_{40}$) nanoparticles for remediation of dye-contaminated water: kinetics and comparison with artificial UV and visible light-mediated photocatalysis. *Environmental Science and Pollution Research*, *25*, pp.13881-13893.

[31] Kalikeri, S. and Shetty Kodialbail, V., **2021.** Auto-combustion synthesis of narrow band-gap bismuth ferrite nanoparticles for solar photocatalysis to remediate azo dye containing water. *Environmental Science and Pollution Research*, *28*(10), pp.12144-12152.

[32] Iqbal, M.A., Ali, S.I., Amin, F., Tariq, A., Iqbal, M.Z. and Rizwan, S., **2019**. La-and Mn-codoped Bismuth Ferrite/Ti_3C_2 MXene composites for efficient photocatalytic degradation of Congo Red dye. *ACS Omega*, *4*(5), pp.8661-8668.

[33] Ponraj, C., Vinitha, G. and Daniel, J., **2017.** A review on the visible light active BiFeO3 nanostructures as suitable photocatalyst in the degradation of different textile dyes. *Environmental Nanotechnology, Monitoring & Management*, *7*, pp.110-120.

[34] Li, J., Wang, Y., Ling, H., Qiu, Y., Lou, J., Hou, X., Bag, S.P., Wang, J., Wu, H. and Chai, G., **2019.** Significant enhancement of the visible light photocatalytic properties in 3D $BiFeO_3$/graphene composites. *Nanomaterials*, *9*(1), p.65.

[35] Bharathkumar, S., Sakar, M. and Balakumar, S., **2015.** Versatility of electrospinning in the fabrication of fibrous mat and mesh nanostructures of bismuth ferrite ($BiFeO_3$) and their magnetic and photocatalytic activities. *Physical Chemistry Chemical Physics*, *17*(27), pp.17745-17754.

[36] Cadenbach, T., Benitez, M.J., Morales, A.L., Vera, C.C., Lascano, L., Quiroz, F., Debut, A. and Vizuete, K., **2020.** Nanocasting synthesis of $BiFeO_3$ nanoparticles with enhanced visible-light photocatalytic activity. *Beilstein journal of nanotechnology*, *11*(1), pp.1822-1833.

[37] Wang, F., Chen, D., Zhang, N., Wang, S., Qin, L., Sun, X. and Huang, Y., **2017.** Oxygen vacancies induced by zirconium doping in bismuth ferrite nanoparticles for enhanced photocatalytic performance. *Journal of Colloid and Interface Science*, *508*, pp.237-247.

[38] Li, Y.A., Li, J., Chen, L., Sun, H., Zhang, H., Guo, H. and Feng, L., **2019.** In situ synthesis of au-induced hierarchical nanofibers/nanoflakes structured $BiFeO_3$ homojunction photocatalyst with enhanced photocatalytic activity. *Frontiers in Chemistry*, *6*, p.649.

[39] Cai, X., Li, J., Liu, Y., Hu, X., Tan, X., Liu, S., Wang, H., Gu, Y. and Luo, L., **2020.** Design and preparation of chitosan-crosslinked bismuth ferrite/biochar coupled magnetic material for methylene blue removal. *International Journal of Environmental Research and Public Health*, *17*(1), p.6.

[40] Li, S., Lin, Y.H., Zhang, B.P., Wang, Y. and Nan, C.W., **2010.** Controlled fabrication of BiFeO3 uniform microcrystals and their magnetic and photocatalytic behaviors. *The Journal of Physical Chemistry C*, *114*(7), pp.2903-2908.

[41] Prabu, K.M. and Anbarasan, P.M., **2014.** Preparation and Characterization of Silver, Magnesium & Bismuth Doped Titanium Dioxide Nanoparticles for Solar Cell Applications. *International Journal of Science and Research*, *3*(9), pp.132-137.

[42] Wang, M., Cheng, L., Huang, L., Pan, S., Yao, Q., Hu, C., Liang, Q. and Zhou, H., **2021.** Effect of Sr doped the $YFeO_3$ rare earth ortho-ferrite on structure, magnetic properties, and microwave absorption performance. *Ceramics International*, *47*(24), pp.34159-34169.

[43] Verma, R., Chauhan, A., Batoo, K.M., Kumar, R., Hadhi, M. and Raslan, E.H., **2021.** Effect of calcination

 © Ariston Publications 2024. All rights reserved

temperature on structural and morphological properties of bismuth ferrite nanoparticles. *Ceramics International*, *47*(3), pp.3680-3691.

[44] Sharma, R., Thakur, P., Sharma, P. and Sharma, V., **2017.** Ferrimagnetic Ni^{2+} doped Mg-Zn spinel ferrite nanoparticles for high density information storage. *Journal of Alloys and Compounds*, *704*, pp.7-17.

[45] Shoushtari, M.Z., Emami, A. and Ghahfarokhi, S.E.M., **2016.** Effect of bismuth doping on the structural and magnetic properties of zinc-ferrite nanoparticles prepared by a microwave combustion method. *Journal of Magnetism and Magnetic Materials*, *419*, pp.572-579.

[46] Irfan, S., Rizwan, S., Shen, Y., Tomovska, R., Zulfiqar, S., Sarwar, M.I. and Nan, C.W., **2016.** Mesoporous template-free gyroid-like nanostructures based on La and Mn co-doped bismuth ferrites with improved photocatalytic activity. *RSC Advances*, *6*(115), pp.114183-114189.

[47] Zhong, X., Zou, Z.S., Wang, H.L., Huang, W. and Zhou, B.X., **2019.** Enhanced activation of persulfate by Co-doped bismuth ferrite nanocomposites for degradation of levofloxacin under visible light irradiation. *Materials*, *12*(23), p.3952.

[48] Rouhani, Z., Karimi-Sabet, J., Mehdipourghazi, M., Hadi, A. and Dastbaz, A., **2019.** Response surface optimization of hydrothermal synthesis of Bismuth ferrite nanoparticles under supercritical water conditions: Application for photocatalytic degradation of Tetracycline. *Environmental Nanotechnology, Monitoring & Management*, *11*, p.100198.

[49] Sakar, M., Balakumar, S., Saravanan, P. and Jaisankar, S.N., **2013.** Annealing temperature mediated physical properties of bismuth ferrite ($BiFeO_3$) nanostructures synthesized by a novel wet chemical method. *Materials Research Bulletin*, *48*(8), pp.2878-2885.

[50] Tomina, E.V., Perov, N.S., Mittova, I.Y., Alekhina, Y.A., Stekleneva, O.V. and Kurkin, N.A., **2020.** Microwave synthesis and magnetic properties of bismuth ferrite nanopowder doped with cobalt. *Russian Chemical Bulletin*, *69*, pp.941-946.

© Ariston Publications 2024. All rights reserved.